SUPPLEMENTAL MATERIAL for:

What drives Fe depletion in calc-alkaline magma differentiation: insights from Fe isotopes

De-Hong Du[1], Ming Tang[2], Weiqiang Li[1], Suzanne Mahlburg Kay[3], Xiao-Lei Wang[1]*

[1]State Key Laboratory for Mineral Deposits Research, School of Earth Sciences and Engineering, Nanjing University, Nanjing 210023, China

[2] Key Laboratory of Orogenic Belt and Crustal Evolution, MOE; School of Earth and Space Sciences, Peking University, Beijing 100871, China

[3]Department of Earth and Atmospheric Sciences, Cornell University, Ithaca, NY 14850, USA

* E-mail: wxl@nju.edu.cn (XL Wang);

1. Analytical Method

The Fe isotope compositions of the whole-rock samples were measured at State Key Laboratory for Mineral Deposits Research, Nanjing University, China. The purification and analytical methods have been described in detail by Du et al. (2017) and Ye et al. (2017). Briefly, ~20 mg of sample powder was dissolved in Teflon beakers using a 2:1:1 mixture of concentrated HCl–HNO_3–HF on a hotplate for two days. The digested samples were purified using ion-exchange chemistry with a chloride-form AG MP-1 anion-exchange resin. The resulting purified Fe solutions were measured using multicollector–inductively coupled plasma–mass spectrometry (MC–ICP–MS) employing a Thermo Fisher Scientific Neptune Plus instrument with moderate resolution and used in the wet-plasma mode. The resulting sensitivity was 6 – 10 V/ppm for ^{56}Fe, with a 2 ppm Fe solution used during analysis. A standard–sample–standard bracketing method was used to correct for mass bias and instrument drift, and iron isotope compositions are reported as the per mil deviation ($\delta^{56}Fe$) from the international standard IRMM-014 ($\delta^{56}Fe_{sample} = [(^{56}Fe/^{54}Fe)_{sample} / (^{56}Fe/^{54}Fe)_{IRMM-014} - 1] \times 1000$ [‰]). Analytical reproducibility on $\delta^{56}Fe$ is better than ±0.06‰ (2 standard deviations, 2SD) based on repeated analyses of several international standards against an in-house stock solution (Du et al., 2017; Ye et al., 2017; Huang et al., 2021). The measured GSP-2 and w-2a geological standards, which were purified and measured together with samples in this study, yield $\delta^{56}Fe$ values of 0.16 ± 0.04‰ ($\delta^{57}Fe = 0.20 \pm 0.09$‰, n = 4, 2SD) and 0.07 ± 0.04‰ ($\delta^{57}Fe = 0.10 \pm 0.13$‰, n = 6, 2SD), consistent with the published values (e.g., Craddock and Dauphas, 2011; He et al., 2015). In addition, $\delta^{56}Fe$ of two ultrapure Fe solutions, J-M and HPS Fe, are 0.34 ± 0.04‰ ($\delta^{57}Fe = 0.51 \pm 0.08$‰, n = 5, 2SD) and 0.59 ± 0.06‰ ($\delta^{57}Fe = 0.84 \pm 0.15$‰, n = 5, 2SD), which are also in excellent agreements with the recommended values (Beard et al., 2003; Heimann et al., 2008). For the samples investigated in this study, each sample was measured at least three times, and analytical uncertainties of Fe isotope ratios were given as 2 SD. The uncertainties on $\delta^{57}Fe$ are much higher than those on $\delta^{56}Fe$. This is due to the limitation of counting statistics of low signal of ^{57}Fe (<0.3 V for typical session).

Crystal fractionation modelling based on pMELTS

In order to evaluate the role of pressure (crustal thickness) on Fe isotope fractionation and trace-element (i.e., Sm/Yb ratio) evolution of arc magmas, we use pMELTS program (Ghiorso et al., 2002) to predict how residual melt and complementary cumulate relate in equilibrium for a range of pressures (0.2–2.0 GPa, the pressure step was set as 0.1 GPa) and oxygen fugacities (from QFM – 1 to QFM + 1). A primitive arc magma from Andean CVZ, defined by Schmidt and Jagoutz (2017), was used as the starting composition, i.e., AN-73 (volatile-free): 53.82 wt% SiO_2, 1.18 wt% TiO_2, 15.88 wt% Al_2O_3, 7.68 wt% FeO_T, 0.13 wt% MnO, 8.24 wt% MgO, 8.29 wt% CaO, 2.78 wt% Na_2O, 1.71 wt% K_2O, and 0.28 wt% P_2O_5. For simplicity, we referred to '**Initial Composition A**' for this primitive arc magma in the latter section. Initial water content was set as 3 wt%. For comparison, we also tested a higher initial water content of 4 wt%. Simulations were conducted for closed-system batch crystallization starting from the liquidus temperature and decreasing at 5 °C steps. At each step, the compositions and respective mass of residual melt and minerals in equilibrium were obtained.

With the coexisting mineral assemblages, we calculated the bulk Sm and Yb partition coefficients between minerals and melt based on the definition of a bulk partition coefficient:

$$D = x_1 Kd_1 + x_2 Kd_2 + x_3 Kd_3 \dots \qquad (1),$$

where Kd is the mineral/melt partition coefficient and x_i refers to the mass fraction of a particular mineral out of the total crystallized assemblages. The partition coefficients for different minerals used in the modeling are given in Table S2. We then calculated the evolution of Sm and Yb in the evolving melt based on Rayleigh fractionation model, with Sm and Yb concentrations in evolving melt (C) given as:

$$\frac{C}{C_0} = F^{(D-1)} \qquad (2),$$

where F is the mass fraction of residual melt, and C_0 is the initial concentrations of Sm and Yb. We assumed that the initial melt has Sm and Yb concentrations of 4 ppm and 2 ppm (i.e., Sm/Yb = 2), respectively.

The Fe isotope evolution of the melt ($\delta^{56}Fe_{melt}$) was calculated using the Rayleigh fractionation model:

$$\delta^{56}Fe_{melt} = \delta^{56}Fe_{initial} + \Delta^{56}Fe_{crystals-melt} \times \ln(f_{Fe}) \qquad (3),$$

where the fraction of iron remaining in the melt is $f_{Fe} = \frac{F \times C_{melt}^{FeO}}{C_{inital}^{FeO}}$ (F and C refer to the melt fraction and Fe content, respectively), and $\Delta^{56}Fe_{crystals-melt}$ is the fractionation factor between the residual melt and the minerals removed. The $\Delta^{56}Fe_{crystals-melt}$ is obtained with the equation:

$$\Delta^{56}Fe_{crystals-melt} = \sum_i (\Delta^{56}Fe_{mineral-melt}^i \times W^i) \tag{4},$$

where $\Delta^{56}Fe_{mineral-melt}^i$ is the fractionation factor between a specific mineral i and the residual melt, and W^i is the iron fraction of mineral i to the bulk cumulate ($\sum_i W^i = 1$). The fractionation factors ($\Delta^{56}Fe_{mineral-melt}^i$) used in the modeling are listed in Table S1. The initial arc melt is assumed to have a $\delta^{56}Fe$ value of 0.05‰.

In addition, another starting composition equivalent to an arc basalt from the Central Andes database (GEOROC) was also assumed (volatile-free; 51.17 wt% SiO_2, 1.89 wt% TiO_2, 15.49 wt% Al_2O_3, 9.00 wt% FeO_T, 0.15 wt% MnO, 7.28 wt% MgO, 8.12 wt% CaO, 3.77 wt% Na_2O, 2.11 wt% K_2O, and 0.82 wt% P_2O_5). We referred to '**Initial Composition B**' for this starting composition. The '**Initial Composition B**' differs from '**Initial Composition A**' with higher FeO_T but lower SiO_2 and MgO contents.

All the modeling studies are summarized below:

Parental melt	Reference	Initial H$_2$O (wt%)	P (GPa)	fO_2	Figure
Initial Composition A	Schmidt and	3	2–0.2	QFM + 1	Fig. 3B, D
Initial Composition A	Jagoutz	3 & 4	2–0.2	QFM + 1	Fig. S1
Initial Composition A	(2017)	3 & 4	2–0.2	QFM	Fig. S2
Initial Composition A		3 & 4	2–0.2	QFM − 1	Fig. S3
Initial Composition B	GEOROC	3	2–0.2	QFM + 1	Fig. S4
Initial Composition B	database	3	2–0.2	QFM	Fig. S5
Initial Composition B		3	2–0.2	QFM − 1	Fig. S6

These modeling results indicate that the arc magma $\delta^{56}Fe$ gradually increases with increasing crustal thickness under more oxidized states (e.g., $\geq$ QFM), regardless of the starting compositions.

Interpretation of the high δ^{56}Fe in the younger "Normal Crust" samples

The younger "Normal Crust" samples (18–10 Ma) have higher δ^{56}Fe values than the older "Normal Crust" samples (> 19 Ma). All the "Normal Crust" samples have low and relatively homogeneous Sm/Yb ratios, indicating they did not experience garnet fractionation. Four candidate mechanisms may explain the higher δ^{56}Fe signatures of the younger "Normal Crust" samples: (1) higher degrees of magmatic differentiation; (2) similar degrees of differentiation at different in fO_2 and water contents; (3) higher degrees of crustal contamination; or (4) Fe isotopically heavier sources. The younger and older samples are very similar in indexes of magma differentiation, including major (e.g., SiO_2, MgO, FeO_T; Fig. 3A) and trace element indicators (e.g., Cr, Ni, La/Yb and Sm/Yb; Fig. 3B; Fig. S7A, B). These suggest that they experienced comparable extents of magma differentiation, eliminating mechanism (1). At low fO_2 (i.e., QFM – 1) and low water content (e.g., 3 wt%), clinopyroxene and olivine are the dominant Fe-bearing minerals under mediate to low pressures (< ~25 km), and fractionation of these two phases can increase δ^{56}Fe in residual melts up to ~0.13‰ (at 50 wt% crystallinity; Fig. S3B, Fig. S6B), similar to those of the younger "Normal Crust" samples. However, fractionation of clinopyroxene and olivine cannot lead to clear Fe depletion (e.g., Sossi et al., 2012; Tang et al., 2018). Under hydrous (e.g., 4 wt% initial water content) and oxidizing conditions, amphibole and magnetite fractionations can explain the moderate Fe depletion (e.g., Kay et al., 1991; Kay and Mpodozis, 2001; Zimmer et al., 2010), but they cannot produce the higher δ^{56}Fe values (Fig. 1C). These indicate that mineral fractionation under low to mediate pressures (i.e., without garnet saturation) hardly explain simultaneous Fe depletion and high δ^{56}Fe signatures of the younger "Normal Crust" magmas. Increasing crustal contamination should be reflected in the ratios such as Th/La and Ba/Th (Kay et al., 2013). However, the younger "Normal crust" samples have Th/La and Ba/Th ratios broadly identical to those of the older "Normal Crust" samples (Fig. S7C, D), indicating that crustal contamination is not responsible for the higher δ^{56}Fe signatures.

Magma differentiation (i.e., partial melting and fractional crystallization) cannot explain the high δ^{56}Fe values of the younger "Normal Crust" samples, and thus an additional contribution from some isotopically heavy materials is required, such as magnetite-bearing cumulates and

metasomatized mantle peridotites. Magnetite-bearing cumulates formed via earlier arc magma differentiation tend to enrich in heavy Fe isotopes. To test this possibility, we calculated the δ^{56}Fe evolution of cumulate based on pMELTS modeling results of hydrous basalt crystal fractionation under 0.2–2.0 GPa, 3 wt% initial water content, and a constant fO_2 of QFM + 1. As shown in Fig. S8, magnetite-bearing cumulates formed at ~25–40 km depths have δ^{56}Fe values ranging from ~0.04‰ to –0.02 ‰ , slightly lower than the mean value of unmetasomatised upper mantle lherzolite (0.033 ± 0.01‰, 2SE; Sossi et al., 2016). Thus, incorporating of these magnetite-bearing cumulates into arc magmas and/or their sources cannot explain the high δ^{56}Fe values of the "Normal Crust" samples. In addition, Weyer and Ionov (2007) indicated that the Fe isotope composition of mantle peridotites could be significantly modified by metasomatic processes (e.g., melt percolation), which lead to an increase in δ^{56}Fe values up to 0.16‰. In this regard, metasomatized peridotites are the possible sources that elevate the δ^{56}Fe values of the younger "Normal Crust" lavas.
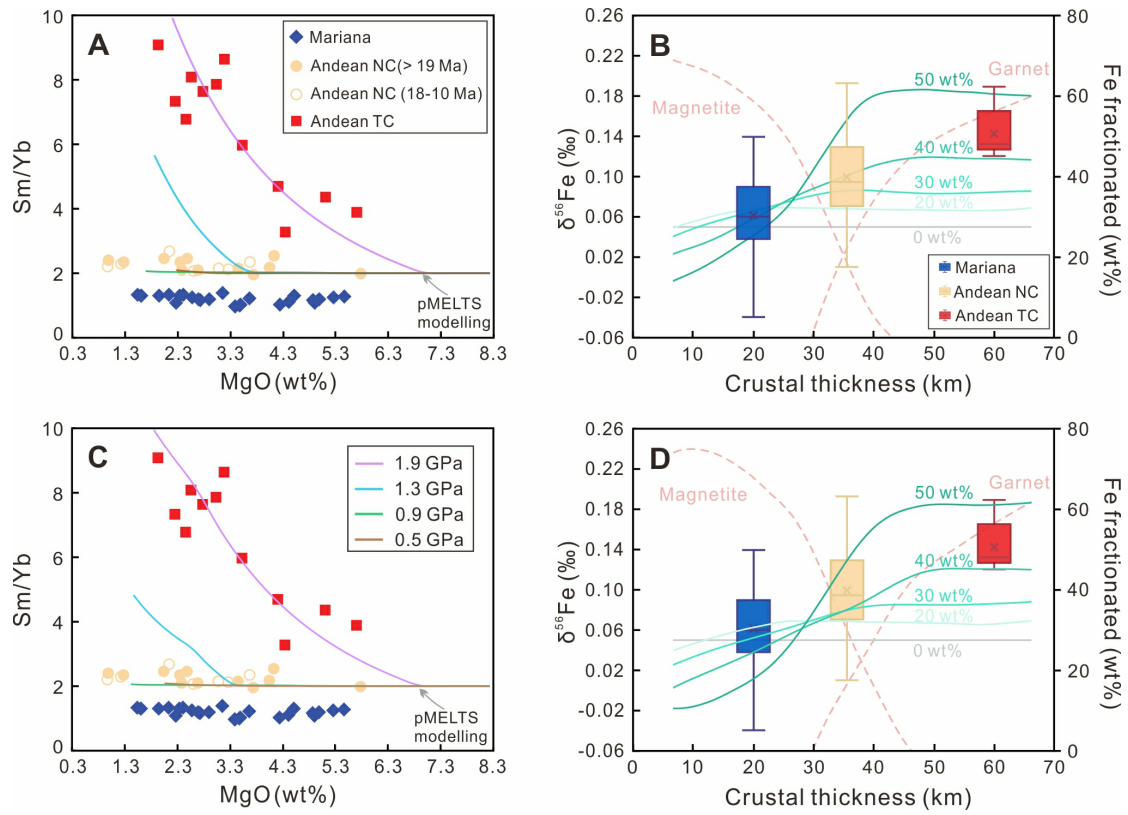
Fig. S1. Modeled pressure effect on melt Sm/Yb (A, C) and $\delta^{56}Fe$ (B, D) during arc magma differentiation. The modeling results are from pMELTS simulation of 'Initial Composition A' crystal fractionation under 0.2 to 2.0 GPa, 3 wt% (A, B) and 4 wt% (C, D) initial water contents, and a constant fO_2 of QFM + 1. The pressure can be converted to crustal thickness based on the equation of thickness (km) $\approx$ 3.3 (km/kbar) $\times$ pressure (kbar). The dashed lines in (B) and (D) represent the iron fraction of magnetite/garnet to the bulk cumulate after 50 wt% crystallization. The solid lines in (B) and (D) are magma $\delta^{56}Fe$ evolution paths from 0 to 50 wt% crystallinity. The initial arc melt is assumed to have a $\delta^{56}Fe$ value of 0.05‰ (Foden et al., 2018).
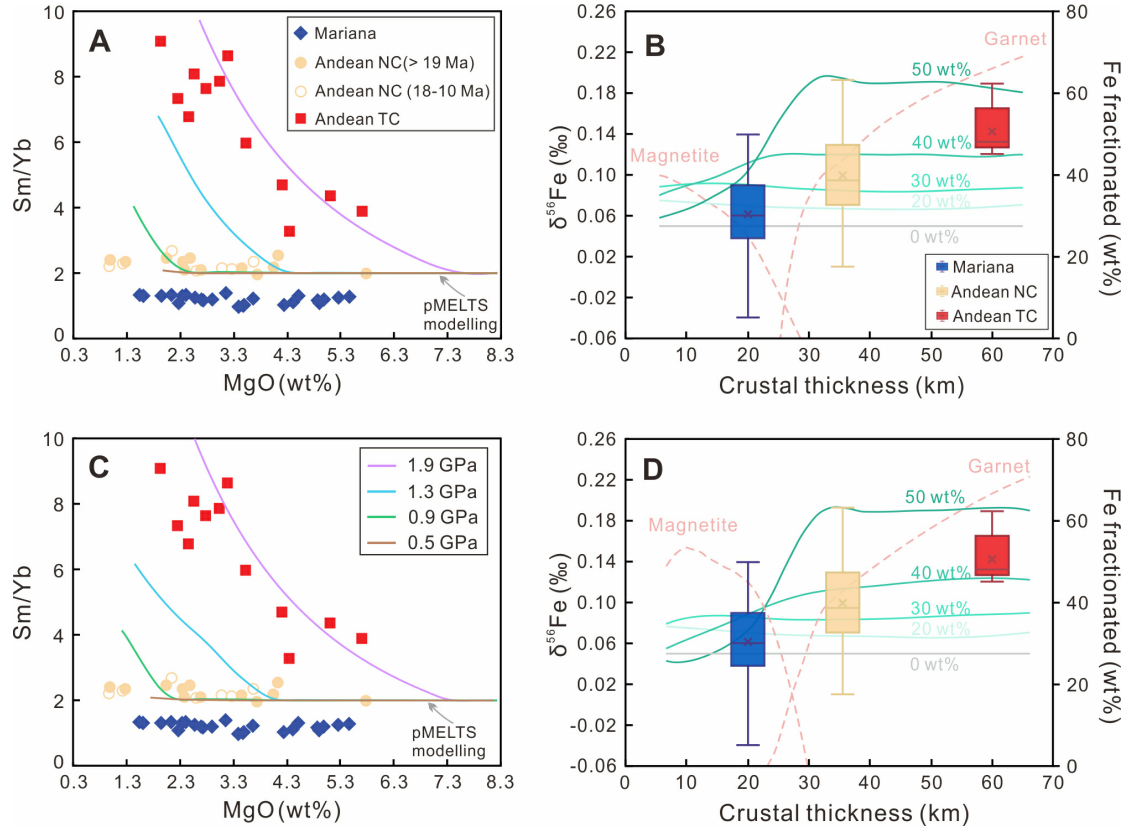
Fig. S2. Modeled pressure effect on melt Sm/Yb (A, C) and $\delta^{56}Fe$ (B, D) during arc magma differentiation. The modeling results are from pMELTS simulation of '**Initial Composition A**' crystal fractionation under 0.2 to 2.0 GPa, 3 wt% (A, B) and 4 wt% (C, D) initial water contents, and a constant fO$_2$ of **QFM**. The dashed lines in (B) and (D) represent the iron fraction of magnetite/garnet to the bulk cumulate after 50 wt% crystallization. The solid lines in (B) and (D) are magma $\delta^{56}Fe$ evolution paths from 0 to 50 wt% crystallinity. The initial arc melt is assumed to have a $\delta^{56}Fe$ value of 0.05‰ (Foden et al., 2018).
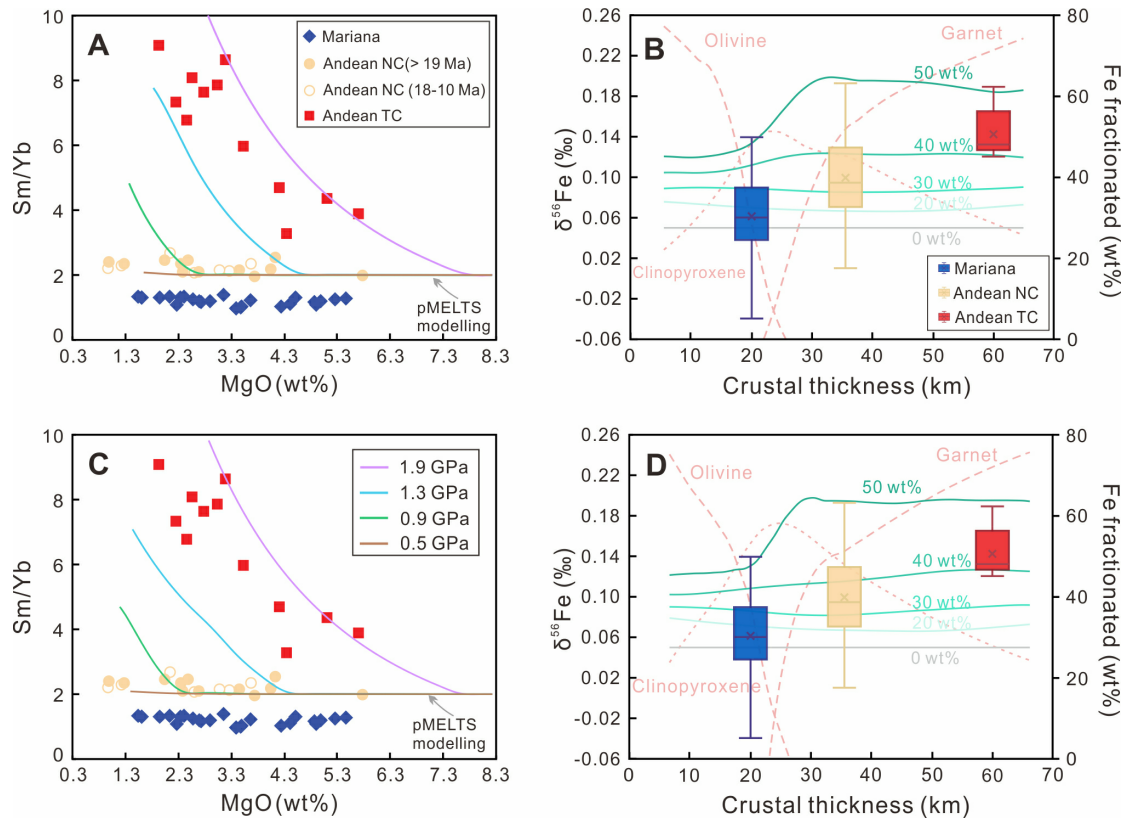
Fig. S3. Modeled pressure effect on melt Sm/Yb (A, C) and $\delta^{56}Fe$ (B, D) during arc magma differentiation. The modeling results are from pMELTS simulation of '**Initial Composition A**' crystal fractionation under 0.2 to 2.0 GPa, 3 wt% (A, B) and 4 wt% (C, D) initial water contents, and a constant fO_2 of **QFM − 1**. The dashed lines in (B) and (D) represent the iron fraction of magnetite/clinopyroxene/garnet to the bulk cumulate after 50 wt% crystallization. The solid lines in (B) and (D) are magma $\delta^{56}Fe$ evolution paths from 0 to 50 wt% crystallinity. The initial arc melt is assumed to have a $\delta^{56}Fe$ value of 0.05‰ (Foden et al., 2018).
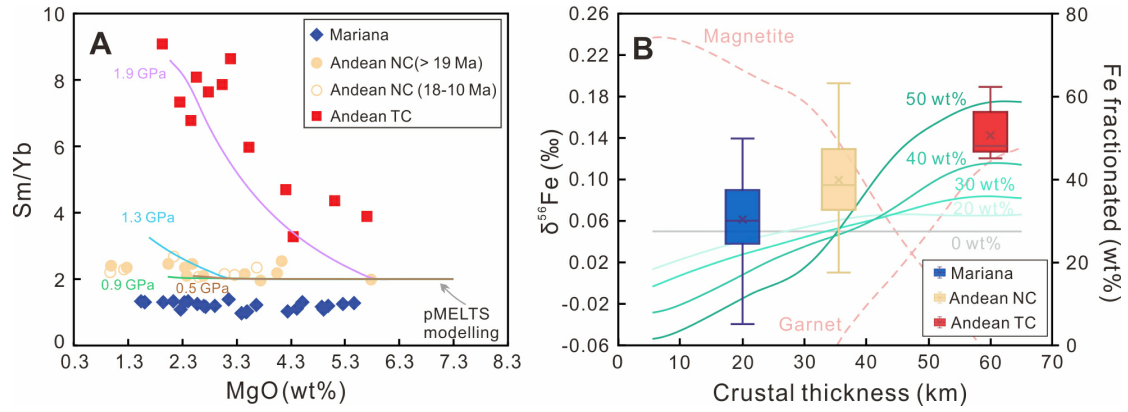
Fig. S4. Modeled pressure effect on melt Sm/Yb (A) and δ^{56}Fe (B) during arc magma differentiation. The modeling results are from pMELTS simulation of 'Initial Composition B' crystal fractionation under 0.2 to 2.0 GPa, 3 wt% initial water content, and a constant fO_2 of QFM + 1. The dashed lines in (B) represent the iron fraction of magnetite/garnet to the bulk cumulate after 50 wt% crystallization. The solid lines in (B) are magma δ^{56}Fe evolution paths from 0 to 50 wt% crystallinity. The initial arc melt is assumed to have a δ^{56}Fe value of 0.05‰ (Foden et al., 2018).

Fig. S5. Modeled pressure effect on melt Sm/Yb (A) and δ^{56}Fe (B) during arc magma differentiation. The modeling results are from pMELTS simulation of 'Initial Composition B' crystal fractionation under 0.2 to 2.0 GPa, 3 wt% initial water content, and a constant fO_2 of QFM. The dashed lines in (B) represent the iron fraction of magnetite/garnet to the bulk cumulate after 50 wt% crystallization. The solid lines in (B) are magma δ^{56}Fe evolution paths from 0 to 50 wt% crystallinity. The initial arc melt is assumed to have a δ^{56}Fe value of 0.05‰ (Foden et al., 2018).

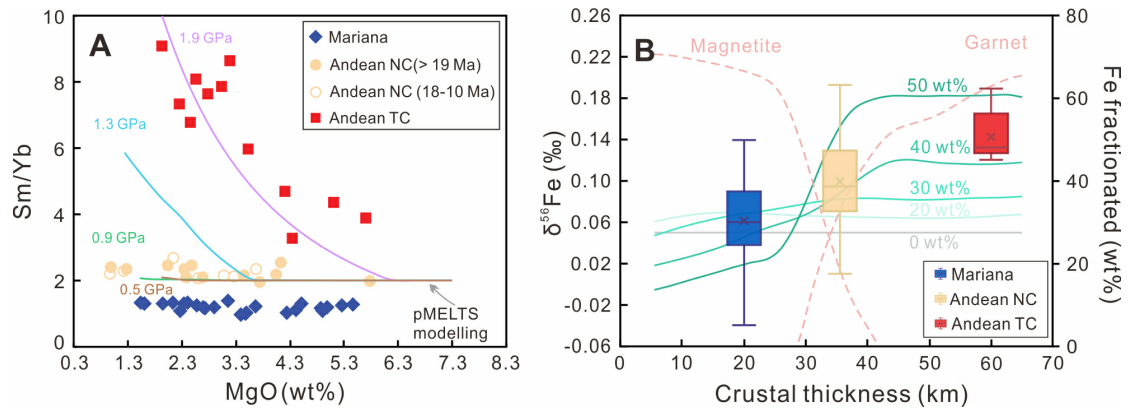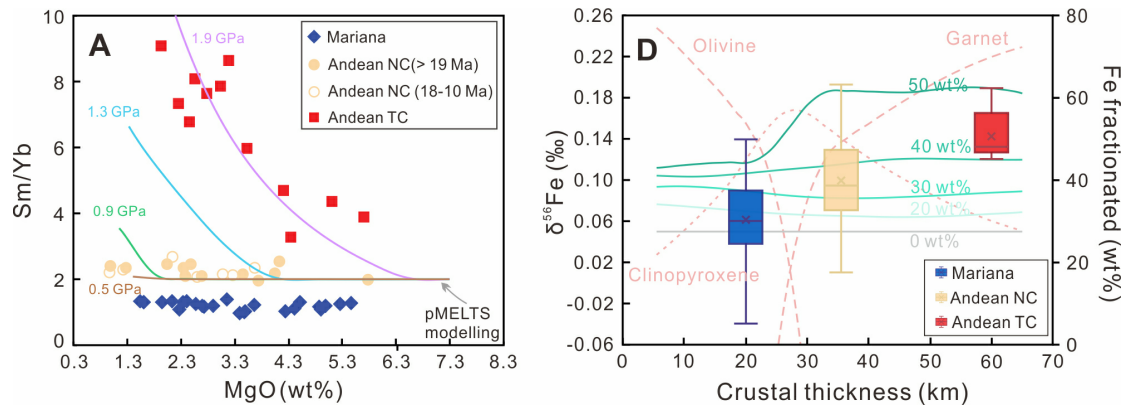Fig. S6. Modeled pressure effect on melt Sm/Yb (A) and δ^{56}Fe (B) during arc magma differentiation. The modeling results are from pMELTS simulation of 'Initial Composition B' crystal fractionation under 0.2 to 2.0 GPa, 3 wt% initial water content, and a constant fO_2 of QFM − 1. The dashed lines in (B) represent the iron fraction of olivine/clinopyroxene/garnet to the bulk cumulate after 50 wt% crystallization. The solid lines in (B) are magma δ^{56}Fe evolution paths from 0 to 50 wt% crystallinity. The initial arc melt is assumed to have a δ^{56}Fe value of 0.05‰ (Foden et al., 2018).
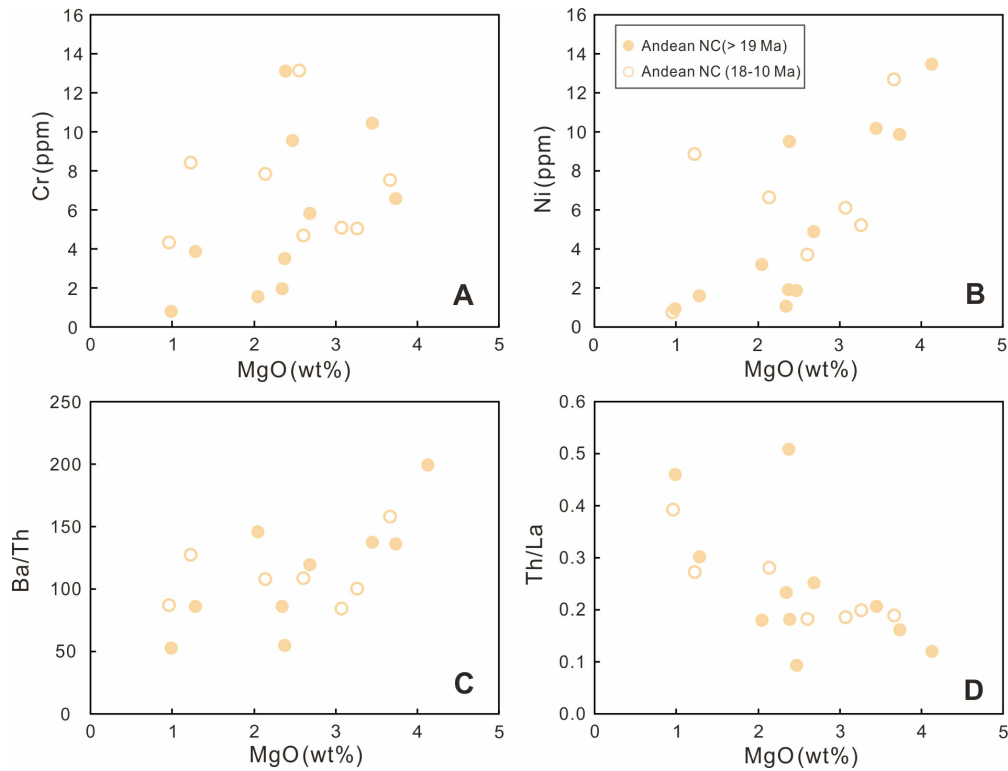

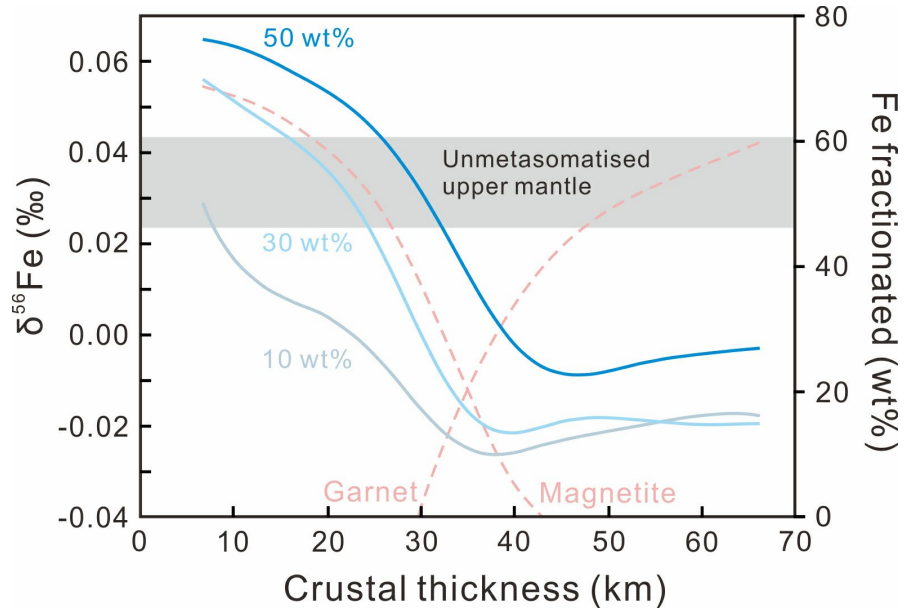Fig. S7. A–D show Cr (ppm), Ni (ppm), Ba/Th and Th/La versus MgO (wt%) for the Andean "Normal Crust" samples.

Fig. S8. Modeled pressure effect on cumulate $\delta^{56}Fe$ during arc magma differentiation. The modeling results are from pMELTS simulation of '**Initial Composition A**' crystal fractionation under 0.2 to 2.0 GPa, 3 wt% initial water content, and a constant fO_2 of **QFM + 1**. The dashed lines represent the iron fraction of magnetite/garnet to the bulk cumulate after 50 wt% crystallization. The solid lines are cumulate $\delta^{56}Fe$ evolution paths from 10 to 50 wt% crystallinity. The initial arc melt is assumed to have a $\delta^{56}Fe$ value of 0.05‰ (Foden et al., 2018). The shaded area represents the mean $\delta^{56}Fe$ of unmetasomatised upper mantle lherzolite ($\delta^{56}Fe$ = 0.033 ± 0.01, 2SE; Sossi et al., 2016).
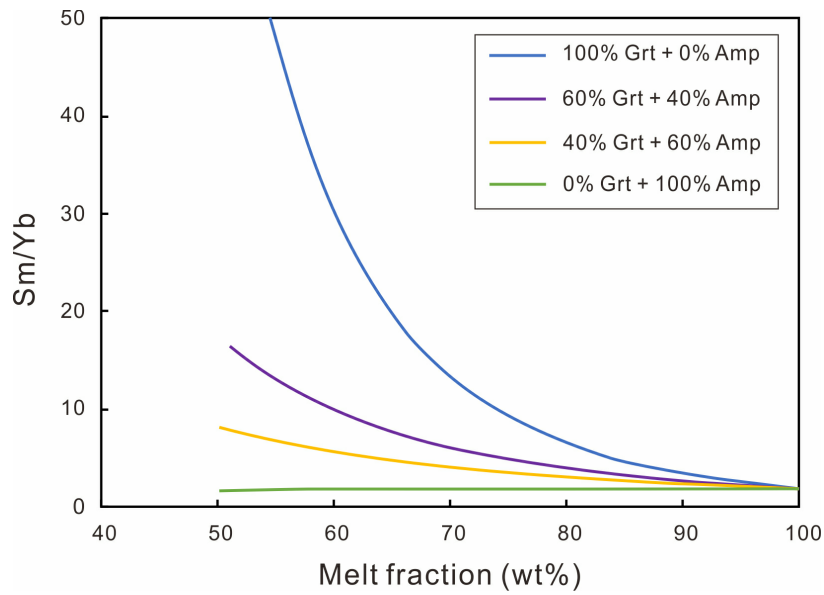

Fig. S9 Effect of amphibole/garnet fractionation on the residual magma's Sm/Yb ratio. The partition coefficients for different minerals used in the modeling are given in Table S2.

Table S1 Compilation of published mineral/melt-magnetite fractionation factors

Type	Phase A	$Fe^{3+}/\Sigma Fe$	CN	$10^3\ln\beta^{56}Fe$	Phase B	$Fe^{3+}/\Sigma Fe$	CN	$10^3\ln\beta^{56}Fe$	$\Delta^{56}Fe_{A-B}$	Temperature (K)	Reference
Rock-calibrated	Grt				Mag				-0.36	$10^6/T^2$	Ye et al., 2020
Experimental	Grt				Mag				-0.44	$10^6/T^2$	Sossi and O'Neill, 2017
Theoretical	Andesitic melt	0.05	5–6	0.57	Mag	0.67	5.33	0.75	-0.19	$10^6/T^2$	Dauphas et al., 2014
Theoretical		0.35	5–6	0.73	Mag	0.67	5.33	0.75	-0.02	$10^6/T^2$	Dauphas et al., 2014
Rock-calibrated	Melt				Mag				-0.13	$10^6/T^2$	Sossi et al., 2012
Theoretical	Ol	0	6	0.56	Mag	0.67	5.33	0.75	-0.19	$10^6/T^2$	Dauphas et al., 2014
Experimental	Fa				Mag				-0.20	$10^6/T^2$	Shahar et al., 2008
Theoretical	Opx	0	6	0.49	Mag	0.67	5.33	0.75	-0.27	$10^6/T^2$	Dauphas et al., 2012
Rock-calibrated	Px				Mag				-0.30	$10^6/T^2$	Sossi et al., 2012
Theoretical	Amp	0.36	6	0.54	Mag	0.67	5.33	0.75	-0.20	$10^6/T^2$	Schoenberg et al., 2009
Rock-calibrated	Amp				Mag				-0.16	$10^6/T^2$	Ye et al., 2020
Calculated	Grt				Melt				-0.23	$10^6/T^2$	
Calculated	Mag				Melt				0.13	$10^6/T^2$	
Calculated	Fa				Melt				-0.07	$10^6/T^2$	
Calculated	Px				Melt				-0.17	$10^6/T^2$	
Calculated	Amp				Melt				-0.03	$10^6/T^2$	

Note: The $10^3\ln\beta^{56}Fe$ for magnetite is from Roskosz et al (2015) and the equilibrium fractionation factor between A and B is calculated as: $\Delta^{56}Fe_{A-B} = 10^3\ln\beta^{56}Fe_A - 10^3\ln\beta^{56}Fe_A$. The calculated mineral-melt Fe isotope fractionation factors are derived by the equation of $\Delta^{56}Fe_{mineral-melt} = \Delta^{56}Fe_{mineral-Mag} + \Delta^{56}Fe_{Mag-melt}$ based on the factors constrained by natural rocks (except for $\Delta^{56}Fe_{Fa-Mag}$, which is constrained by experiment), in which $\Delta^{56}Fe_{melt-Mag}$ is cited as $0.13\times10^6/T^2$ (Sossi et al., 2012). CN = coordination. Abbreviations: Grt = garnet, Ol = olivine, Fa = fayalite, Opx = orthopyroxene, Px = pyroxene, Amp = amphibole, Mag = magnetite.

Table S2 Mineral/melt partition coefficients used in the trace element modeling

Mineral	Element	Kd value	Kd type	Reference
Garnet	Yb	6.1	Experimental	Green et al., 2000
Clinopyroxene	Yb	0.54	Phenocryst-matrix	Dostal et al., 1983
Orthopyroxene	Yb	0.22	Experimental	Green et al., 2000
Biotite	Yb	0.44	Phenocryst-matrix	Higuchi and Nagasawa, 1969
Plagioclase	Yb	0.299	Phenocryst-matrix	Schnetzler and Philpotts, 1970
Magnetite	Yb	0.24	Phenocryst-matrix	Luhr and Carmichael, 1980
Olivine	Yb	0.03	Phenocryst-matrix	Luhr and Carmichael, 1980
Amphibole	Yb	0.44	Experimental	Adam and Green, 2006
Garnet	Sm	0.800	Experimental	Ronov and Yaroshevskiy, 1976
Clinopyroxene	Sm	0.550	Phenocryst-matrix	Dostal et al., 1983
Orthopyroxene	Sm	0.015	Experimental	Green et al., 2000
Biotite	Sm	0.26	Phenocryst-matrix	Higuchi and Nagasawa, 1969
Plagioclase	Sm	0.203	Phenocryst-matrix	Schnetzler and Philpotts, 1970
Magnetite	Sm	0.290	Phenocryst-matrix	Luhr and Carmichael, 1980
Olivine	Sm	0.007	Phenocryst-matrix	Dunn and Sen, 1994
Amphibole	Sm	0.54	Experimental	Adam and Green, 2006

References in the supplementary file

Adam, J., Green, T., 2006, Trace element partitioning between mica-and amphibole-bearing garnet lherzolite and hydrous basanitic melt: 1. Experimental results and the investigation of controls on partitioning behavior: Contributions to Mineralogy and Petrology, v. 152, p. 1–17.

Beard, B.L., Johnson, C.M., Skulan, J.L., Nealson, K.H., Cox, L., and Sun, H., 2003, Application of Fe isotopes to tracing the geochemical and biological cycling of Fe: Chemical Geology, v. 195, p. 87–117.

Craddock, P.R., and Dauphas, N., 2011, Iron isotopic compositions of geological reference materials and chondrites: Geostandards and Geoanalytical Research, v. 35, p. 101–123.

Dauphas, N., Roskosz, M., Alp, E.E., Golden, D.C., Sio, C.K., Tissot, F.L.H., Hu, M.Y., Zhao, J., Gao, L., and Morris, R.V., 2012, A general moment NRIXS approach to the determination of equilibrium Fe isotopic fractionation factors: application to goethite and jarosite: Geochimica et Cosmochimica Acta, v. 94, p. 254–275.

Dauphas, N., Roskosz, M., Alp, E.E., Neuville, D.R., Hu, M.Y., Sio, C.K., Tissot, F.L.H., Zhao, J., Tissandier, L., Médard, E., and Cordier, C., 2014, Magma redox and structural controls on iron isotope variations in Earth's mantle and crust: Earth and Planetary Science Letters, v. 398, p. 127–140.

Dostal, J., Dupuy, C., Carron, J. P., De Kerneizon, M. L.G., and Maury, R.C., 1983, Partition coefficients of trace elements: application to volcanic rocks of St. Vincent, West Indies: Geochimica et Cosmochimica Acta, v. 47, p. 525–533.

Du, D.H., Wang, X.L., Yang, T., Chen, X., Li, J.Y., and Li, W., 2017, Origin of heavy Fe isotope compositions in high-silica igneous rocks: a rhyolite perspective: Geochimica et Cosmochimica Acta, v. 218, p. 58–72.

Dunn, T., and Sen, C., 1994, Mineral/matrix partition coefficients for orthopyroxene, plagioclase, and olivine in basaltic to andesitic systems: a combined analytical and experimental study: Geochimica et Cosmochimica Acta, v. 58, p. 717–-733.

Foden, J., Sossi, P.A., and Nebel, O., 2018, Controls on the iron isotopic composition of global arc magmas: Earth and Planetary Science Letters, v. 494, p. 190–201.

Ghiorso, M.S., Hirschmann, M.M., Reiners, P.W., and Kress, V.C., III, 2002, The pMELTS: A revision of MELTS for improved calculation of phase relations and major element partitioning related to partial melting of the mantle to 3 GPa: Geochemistry Geophysics Geosystems, v. 3, p. 1–35.

Green, T.H., Blundy, J.D., Adam, J., and Yaxley, G.M., 2000, SIMS determination of trace element partition coefficients between garnet, clinopyroxene and hydrous basaltic liquids at 2–7.5 GPa and 1080–1200 C: Lithos, v. 53, p. 165–187.

He, Y., Ke, S., Teng, F.Z., Wang, T., Wu, H., Lu, Y., and Li, S., 2015, High-precision iron isotope analysis of geological reference materials by high-resolution MC-ICP-MS: Geostandards and Geoanalytical Research, v. 39, p. 341–356.

Heimann, A., Beard, B.L., and Johnson, C.M., 2008, The role of volatile exsolutions and sub-solidus fluid/rock interactions in producing high $^{56}Fe/^{54}Fe$ ratios in siliceous igneous rocks: Geochimica et Cosmochimica Acta, v. 72, p. 4379–4396.

Higuchi, H., and Nagasawa, H., 1969, Partition of trace elements between rock-forming minerals and the host volcanic rocks.: Earth and Planetary Science Letters, v. 7, p. 281–287.

Huang, Q., Viehmann, S., Walde, D. H., and Li, W., 2021, Iron isotope constraints on the metal source and depositional environment of the Neoproterozoic banded iron-and manganese deposits in Urucum, Brazil: Geochemistry, 125771.

Kay, S.M., and Mpodozis, C., 2001, Central Andean ore deposits linked to evolving shallow subduction systems and thickening crust: Geological Society of America Today, v. 11, p. 4–9.

Kay, S.M., Mpodozis, C., and Gardeweg, M., 2013, Magma sources and tectonic setting of Central Andean andesites (25.5–28ºS) related to crustal thickening, forearc subduction erosion and delamination: Geological Society, London, Special Publications, v. 385, p. 303–334.

Kay, S.M., Mpodozis, C., Ramos, V.A., and Munizaga, F., 1991, Magma source variations for mid-late Tertiary magmatic rocks associated with a shallowing subduction zone and a thickening crust in the central Andes (28 to 33 °S): Geological Society of America Special Paper, v. 265, p. 113–137.

Luhr, J.F., and Carmichael, I.S., 1980, The colima volcanic complex, Mexico: Contributions to Mineralogy and Petrology, v. 71, p. 343–372.

Philpotts, J.A., and Schnetzler, C.C., 1970, Apollo 11 lunar samples: K, Rb, Sr, Ba and rare-earth concentrations in some rocks and separated phases: Geochimica et Cosmochimica Acta Supplement, v. 1, p. 1471.

Ronov, A.B., and Yaroshevsky, A.A., 1976, A new model of chemical composition of the Earth crust: Geokhimiya, v. 12, p. 1763.

Schmidt, M.W., and Jagoutz, O., 2017, The global systematics of primitive arc melts: Geochemistry, Geophysics, Geosystems, v. 18, p. 2817–2854.

Schoenberg, R., Marks, M.A., Schuessler, J.A., von Blanckenburg, F., and Markl, G., 2009, Fe isotope systematics of coexisting amphibole and pyroxene in the alkaline igneous rock suite of the Ilímaussaq Complex, South Greenland: Chemical Geology, v. 258, p. 65–77.

Beard, B.L., Johnson, C.M., Skulan, J.L., Nealson, K.H., Cox, L., and Sun, H., 2003, Application of Fe isotopes to tracing the geochemical and biological cycling of Fe:

Chemical Geology, v. 195, p. 87–117.

Shahar, A., Young, E.D., and Manning, C.E., 2008, Equilibrium high-temperature Fe isotope fractionation between fayalite and magnetite: an experimental calibration: Earth and Planetary Science Letters, v. 268, p. 330–338.

Sossi, P.A., and O'Neill, H.S.C., 2017, The effect of bonding environment on iron isotope fractionation between minerals at high temperature: Geochimica et Cosmochimica Acta, v. 196, p. 121–143.

Sossi, P.A., Foden, J.D., and Halverson, G.P., 2012, Redox-controlled iron isotope fractionation during magmatic differentiation: an example from the Red Hill intrusion, S. Tasmania: Contributions to Mineralogy and Petrology, v. 164, p. 757–772.

Sossi, P.A., Nebel, O., and Foden, J., 2016, Iron isotope systematics in planetary reservoirs: Earth and Planetary Science Letters, v. 452, p. 295–308.

Tang, M., Erdman, M., Eldridge, G., and Lee, C.-T.A., 2018, The redox "filter" beneath magmatic orogens and the formation of continental crust: Science Advances, v. 4, p. eaar4444.

Weyer, S., and Ionov, D.A., 2007, Partial melting and melt percolation in the mantle: the message from Fe isotopes: Earth and Planetary Science Letters, v. 259, p. 119–133.

Williams, H.M., Prytulak, J., Woodhead, J.D., Kelley, K.A., Brounce, M., and Plank, T., 2018, Interplay of crystal fractionation, sulfide saturation and oxygen fugacity on the iron isotope composition of arc lavas: an example from the Marianas: Geochimica et Cosmochimica Acta, v. 226, p. 224–243.

Ye, H., Wu, C.Z., Yang, T., Santosh, M., Yao, X.Z., Gao, B.F., Wang, X.L., and Li, W., 2017, Updating the geologic barcodes for south China: discovery of late archean banded iron formations in the Yangtze craton: Scientific Report, v. 7, p. 15082.

Ye, H., Wu, C., Brzozowski, M.J., Yang, T., Zha, X., Zhao, S., Gao, B., and Li, W., 2020, Calibrating equilibrium Fe isotope fractionation factors between magnetite, garnet, amphibole, and biotite: Geochimica et Cosmochimica Acta, v. 271, p. 78–95.

Zimmer, M.M., Plank, T., Hauri, E.H., Yogodzinski, G.M., Stelling, P., Larsen, J., Singer, B., Jicha, B., Mandeville, C., and Nye, C.J., 2010, The role of water in generating the calc-alkaline trend: new volatile data for Aleutian magmas and a new tholeiitic index: Journal of Petrology, v. 51, p. 2411–2444.